NANO · MICRO small
www.small-journal.com

Fully Fibrous Large-Area Tailorable Triboelectric Nanogenerator Based on Solution Blow Spinning Technology for Energy Harvesting and Self-Powered Sensing

Huayu Xu, Juan Tao, Yue Liu, Yepei Mo, Rongrong Bao, and Caofeng Pan**

An all-fibrous large-area (20 × 50 cm^2) tailorable triboelectric nanogenerator (LT-TENG) is prepared using a one-step solution blow spinning technology, which has the advantages of easy operation, scale-up in the area, and high production efficiency. The prepared LT-TENG is composed of polyvinylidene fluoride (PVDF)/MXene ($Ti_3C_2T_x$) nanofibers (NFs) and conductive textile. Benefiting from the fibrous materials and large-area properties, the LT-TENG possesses the merits of good tailorability, breathability, hydrophobicity, and washability. When optimized by mixing the MXene into PVDF NFs, the LT-TENG has a preferable output and sensing property, with a detection range over 16 kPa and a relatively high sensitivity of 12.33 V KPa^{-1}. At maximum applied pressure, the voltage, current, and charge are 108 V, 38 μA, and 35 nC, respectively. This LT-TENG can serve as a biomechanical energy harvester when used as wearable devices with an output power density of 12.6 mW m^{-2} at an external load resistance of 500 MΩ, and it also has the ability of self-powered tactile sensing for pressure mapping and slide sensing. Thus, this LT-TENG exhibits great potential prospects in wearable devices, intelligent robots, and human–machine interaction.

1. Introduction

Over the past few decades, with the continuous updating of wearable electronic devices, the progress of nanomaterials and micro-nano in manufacturing has been facilitated to some extent. It has further contributed to developing flexible electronics, especially tactile sensors.[1–4] Up to now, tactile sensors have made significant breakthroughs with novel features such as stretchable,[5–7] self-healing,[8,9] self-powered,[10,11] and multi-functional properties.[12–14] Most of these tactile sensors must require battery storage to provide energy if they continuously collect information. However, constant battery replacement is not conducive to environmental protection. Consequently, to achieve the goal of realizing carbon-neutral, novel energy harvesting approaches or sustainable power sources are available to address these issues. Triboelectric nanogenerator (TENG) was proposed by Wang et al. in 2012 as a new alternative strategy.[15] It can act as an energy harvester by converting mechanical energy into electrical energy from ambient environments and also can be used as a self-powered tactile sensor by generating electric signals.[16–18] Single-electrode mode TENG consisting of a triboelectric dielectric layer and a corresponding conductive electrode has been extensively used in TENG-based device fabrication because of its simple structure and the convenience of carrying.[19,20] Over the past few years, due to the benefits of its low cost, low power consumption, simple structure, lightweight, and abundant material

H. Xu, Y. Mo, R. Bao
School of Chemistry and Chemical Engineering
Guangxi University
Nanning, Guangxi 530004, P. R. China
E-mail: baorongrong@binn.cas.cn

H. Xu, Y. Liu, Y. Mo, R. Bao, C. Pan
CAS Center for Excellence in Nanoscience
Beijing Key Laboratory of Micro-Nano Energy and Sensor
Beijing Institute of Nanoenergy and Nanosystems
Chinese Academy of Sciences
Beijing 100083, P. R. China
E-mail: cfpan@binn.cas.cn

The ORCID identification number(s) for the author(s) of this article can be found under https://doi.org/10.1002/smll.202202477.

DOI: 10.1002/smll.202202477

J. Tao
College of Physics and Optoelectronic Engineering
Shenzhen University
Shenzhen 518060, P. R. China

R. Bao, C. Pan
School of Nanoscience and Technology
University of Chinese Academy of Sciences
Beijing 100049, P. R. China

C. Pan
Center on Nanoenergy Research
School of Physical Science and Technology
Guangxi University
Nanning, Guangxi 530004, P. R. China

selection, remarkable progress has been achieved in TENGs for energy collectors with high energy conversion efficiency and self-powered tactile sensors arrays, which have been widely used in wearable electronic devices.[21–23] Various approaches, including novel materials, micro/nano-structure, and new technology, have been utilized to promote the performance of TENG. Currently, MXene, as a new two dimensional (2D) transition metal carbides and nitrides, has been widely used in different fields such as supercapacitors, shielding films, and gas sensors.[24–26] Compared to other 2D materials, MXene exhibits an excellent metallic electronic conductivity and highly electronegative surface, attributed to the electric negative functional group like −OH and −F. Thus, MXene becomes an alternative to conventional polymeric electronegative materials for TENGs to improve performance.[27–29]

Comfort is an essential factor when applied to wearable devices for interacting with the human body. Nevertheless, most traditional wearable devices are constructed from polymeric block materials or films, suffering from thick or airtight disadvantages.[30,31] Hence, TENGs composed of textile or NFs are conducive to endowing a wearable TENG with the merits of flexibility, permeability, and comfort.[10,32,33] Nanofiber films with tunable physical/chemical properties, variable pore size distribution, and porous structures can be used to prepare self-powered wearable TENGs. Up to now, most fibrous films are prepared by electrostatic spinning technique, but the preparation process requires the use of high voltage, which may cause potential safety hazards. Second, nanofibers prepared by electrostatic spinning are subject to inefficient in area-scalable nanofibers, which limits the integration and practical application in wearable devices.[34,35] Alternatively, as an emerging technology, solution blow spinning (SBS) is a new sub-micron/nanofiber preparation approach based on the principle of high-speed airflow drawing.[36–39] Compared with the electrostatic spinning method, this technique is independent of high voltage and conductive collectors. It has the merits of a convenient process, low energy consumption, scale-up, and high production efficiency.[40,41] At present, the use of SBS technology for the preparation of nanofiber-based TENG is relatively rare.

Herein, we present an all-fibrous LT-TENG array for energy harvesting and self-powered sensing via one-step SBS technology. The PVDF/MXene NFs are directly drawn onto the surface of conductive textile to prepare a fully fibrous single-electrode TENG. The large-area characteristic and fibrous structure enable the TENGs with tailorability, breathability, hydrophobicity, and washable properties. Due to the strong electron-capture ability of MXene, it is utilized to enhance the triboelectric properties of the LT-TENG. Compared with the TENG based on pristine PVDF, TENG composed of PVDF/MXene with the optimal mixed concentrate of 15% can produce a higher open-circuit voltage (Voc) of ≈90 V. When served as a self-powered tactile sensor, it can detect external pressure over 16 KPa with a relatively high sensitivity of 12.33 V KPa^{-1}. Additionally, the prepared LT-TENG can serve as a biomechanical energy harvester when combined with the human body and also can serve as a tactile sensor array for pressure mapping and sliding perceiving. This fully fibrous LT-TENG with superior comfort and wearability exhibit outstanding energy harvesting and sensing capability, demonstrating a prospect in wearable electronics, artificial intelligent robotics, and human–machine interaction.

2. Results and Discussion

The LT-TENG is fabricated by directly blowing PVDF/MXene NFs onto the conductive fabric based on SBS technology, as schematically illustrated in **Figure 1**a. The prepared PVDF/MXene solution is drafted under the high-speed airflow and a roller covered with conductive textile is used to receive the PVDF/MXene fibers with the volatilization of the solution (Figure 1ai). The preparation process of PVDF/MXene solution is detailedly depicted in the Experimental Section. Based on the SBS method, the LT-TENG can reach area-scalable by a rational design of the receiving device. Therefore, except for the basic characteristic of wearability, breathability, and waterproofness, the prepared LT-TENG in this paper possesses the merit of tailorable, which can be potentially cut into various clothing such as gloves, hats, and even sweaters (Figure 1aii).

To improve the output performance of LT-TENG, the 2D material MXene ($Ti_3C_2T_x$) is introduced. It has been confirmed that MXene containing the −F group has good electronegativity. It also has good electrical conductivity compared to commonly used polymers, such as PVDF and Polytetrafluoroethylene, which can increase the surface charge density of the friction layer, thus increasing the dielectric constant and improving the output of TENG. First is the preparation of the MXene nanosheet, which will be further discussed in the Experimental Section. To demonstrate the successful preparation of MXene, the corresponding characteristic has been performed. First, the prepared MXene nanosheets can be well dispersed in water with a significant Tyndall effect (Figure S1, Supporting Information). As shown in Figure 1b, according to the SEM, the synthetic MXene has a distinct multilayer structure with an accordion-like form, which provides a large specific surface area for adhesion of PVDF chains onto the surface. The (002) peak of MXene in the XRD pattern is also shifted to a lower angle ($2\theta = 6.90°$) with a broader peak (Figure 1c). This is because of the increase in the c-lattice parameter and the loss of interlayer correlation caused by the insertion of water molecules and lithium ions. Additionally, the remaining diffraction peaks almost disappeared, especially the strongest diffraction peak located at $2\theta = 39.05°$, indicating that Ti_3AlC_2 is exfoliated into thin nanosheets and Al is completely etched. Furthermore, the Raman spectra of MXene are shown in Figure S2, Supporting Information. The peak at 150 cm^{-1} is A_{1g} mode, which is mainly the out-of-plane vibration of C, Ti, and O. And the peaks at 260, 404, and 600 cm^{-1} are E_g mode, where 260 and 404 cm^{-1} are in-plane vibrations attached to the Ti surface groups, and the peak at 600 cm^{-1} is in-plane vibrations of C. All of the analysis of the above characteristics indicate that MXene is adequately synthesized.

After that, the obtained MXene is directly mixed with PVDF solution, obtaining the PVDF/MXene hybrid solution. The PVDF/MXene NFs have been obtained by the SBS technique at fixed airflow rate, spinning rate, and temperature, with corresponding details discussed further in the Experimental Section. It can be observed that the prepared PVDF/MXene film presents

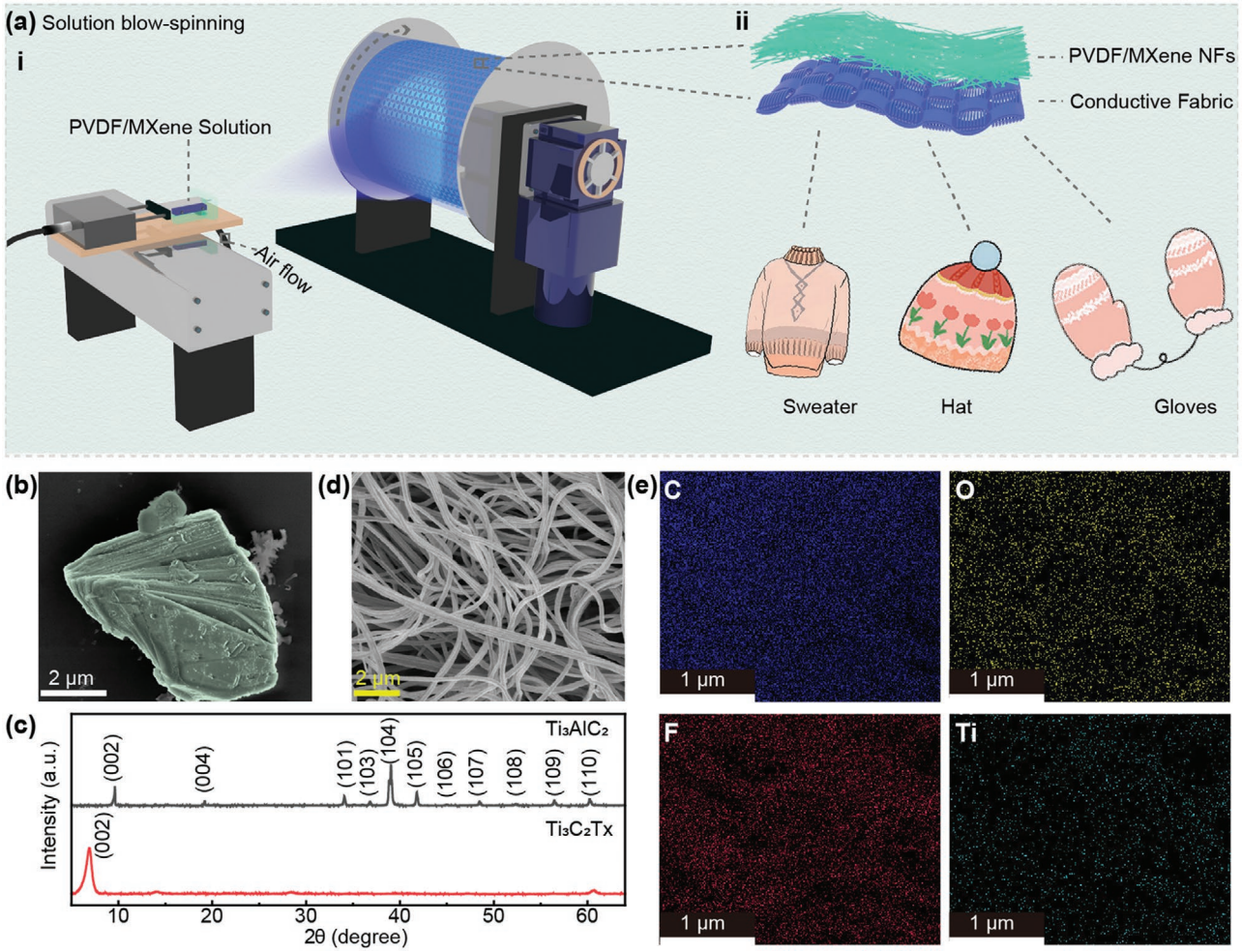

Figure 1. Preparation of the LT-TENG. a) Preparation process schematic diagram of fabricating the LT-TENG based on SBS technology. b) Scanning electron microscopy (SEM) images of MXene nanoflake. c) The X-ray diffraction (XRD) spectra of MAX (Ti_3AlC_2) phase precursor and MXene ($Ti_3C_2T_x$) nanoflake. d) SEM image of PVDF/MXene NFs. e) Energy dispersive spectrometer (EDS) elemental mapping image of the PVDF/MXene NFs.

a porous structure with nanofibers of about 100 ± 10 nm in diameter (Figure 1d). The porous structure attributed to PVDF/MXene NFs can immensely enhance triboelectric friction. At the same time, the multilayer stacked nanofiber network produces a large number of 3D nanolayered pores, which is beneficial to good air permeability for wearable devices. Furthermore, as shown in Figure S3, Supporting Information, the enhanced surface roughness of PVDF/MXene nanofibers is compared to PVDF nanofibers. It may help to improve the effective frictional contact area of TENG. The detailed X-ray photoelectron spectroscopy (XPS) measurement spectra of PVDF/MXene NFs are shown in Figure S4, Supporting Information, and the full spectral analysis revealed the presence of C, F, and O (Figure S4a, Supporting Information). The high-resolution XPS spectra of C 1 s showed four sets of peaks, 284.88, 286.57, 288.75, and 291.04 eV, for C—C, C—O, O—C=O, and C—F bonds, respectively (Figure S4b, Supporting Information). And the high-resolution spectra of O 1 s and F 1 s are also shown in Figures S4c and S4d, Supporting Information, respectively. Figure 1e shows the EDS mapping images of the PVDF/MXene NFs prepared by the SBS method, indicating that C, O, F, and Ti elements are uniformly distributed throughout the nanofiber films. Both Ti and O elements are obtained from MXene nanosheets, while both C and F elements are obtained from PVDF and MXene. The EDS result shows that MXene nanosheets are successfully doped into PVDF/MXene NFs.

After the fabrication of LT-TENG by one-step SBS technology, the properties of its wearable performance are performed. As shown in **Figure 2**a, the fabricated LT-TENG can be easily bent and twisted without any damage after release, demonstrating its good flexibility. Simultaneously, due to the fibrous structure and material property, the prepared LT-TENG would exhibit excellent hydrophobic properties. As seen in Figure 2b, the water contact angle of the conductive fabric electrode is found to be 104° (Figure 2bi), while the PVDF/MXene NFs film is about 122° (Figure 2bii), respectively. As a wearable device, good breathability is also an essential factor. As illustrated in Figure 2c, three different substances, including Polydimethylsiloxane (PDMS), LT-TENG, commercial gauze (the warp and weft density of the gauze was 41 × 36), as well as the blank control group (without any lid), are compared for the air permeability test. The same liquid quality of water has been poured

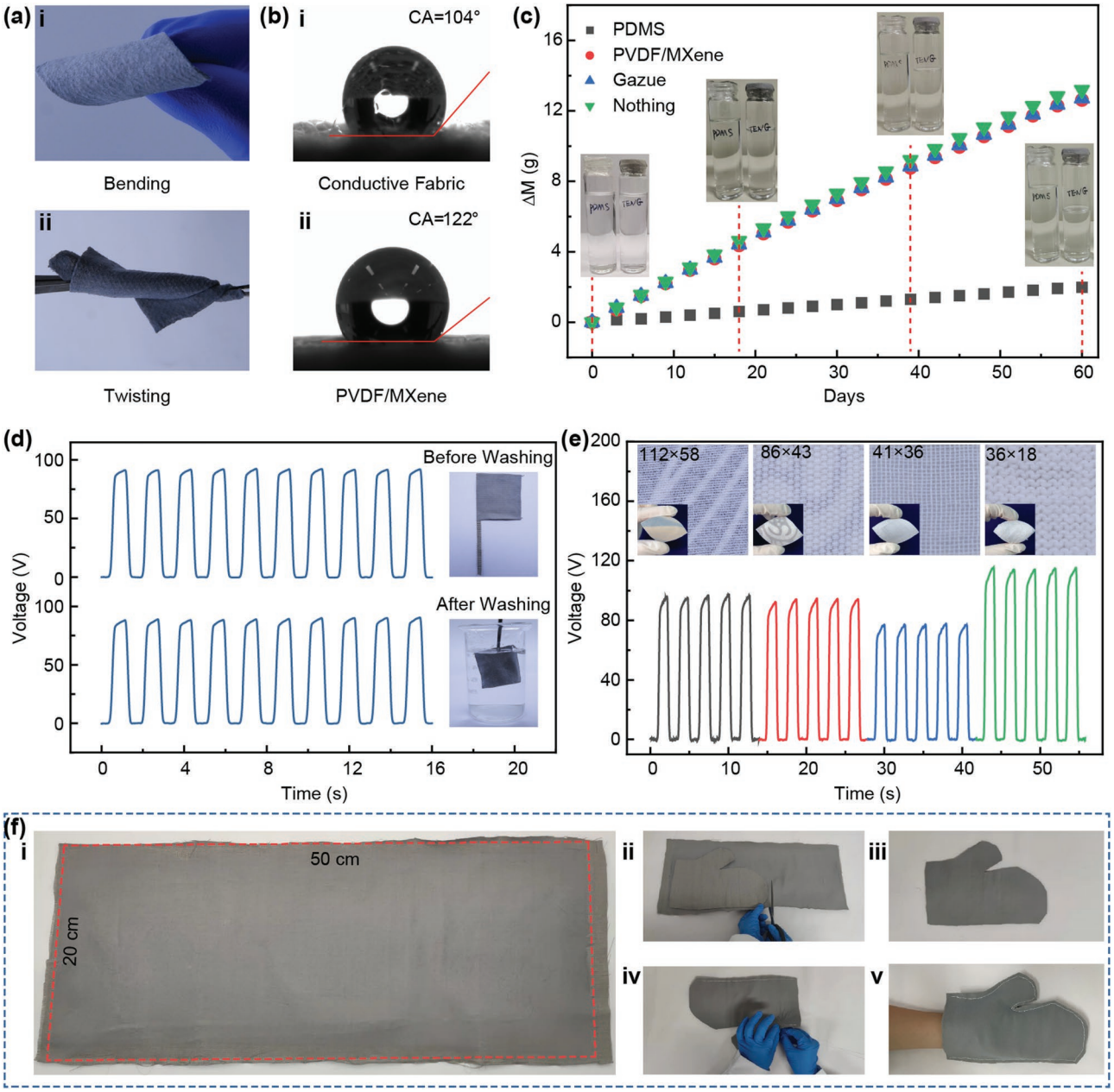

Figure 2. Wearable properties of the LT-TENG. a) Optical images of bending (i) and twisting (ii) of LT-TENG. b) Photograph of LT-TENG internal (i) and external (ii) water contact angle. c) Comparison of air permeability in PDMS, LT-TENG, Gauze, and Nothing. d) Voltage output of LT-TENG before and after water washing. e) Open-circuit voltage of LT-TENG with fabrics of different warp and weft densities as backing. f) The area of LT-TENG is 20 × 50 cm (i), which can be cut into gloves (ii → iii → iv → v).

into four glass bottles, wrapped with PDMS, LT-TENG, and gauze, respectively, and the other bottle maintains open. The difference in weight $\Delta M_{(M\text{-}M0)}$ of that glass is recorded every 3 days from the first day, with the corresponding results shown in Figure 2c. It can be found that the value of ΔM of the LT-TENG is much higher than that of PDMS, and the breathable effect of the LT-TENG is close to that of the gauze and open-ended blank control demonstrating excellent breathability. The photos of differences in liquid level between PDMS, LT-TENG, Gauze, and Nothing on days 1, 18, 39, and 60 are significantly different (inset in Figure 2c and Figure S5, Supporting Information). Therefore, this LT-TENG has the potential to contact with the human skin for a long time without side effects such as inflammation. Furthermore, its washing performance is also tested, which is illustrated in Figure 2d. The open-circuit voltage output of the LT-TENG (with a size of 3 × 3 cm^2) is performed before and after washing. The output voltage was 91 V before washing and 88 V after water washing, with corresponding snapshots shown in the inset of Figure 2d.

SBS technology for preparing full-fibrous TENG is simple, universal, and scalable. Various textile substrates have been used to demonstrate their universality. PVDF/MXene NFs can

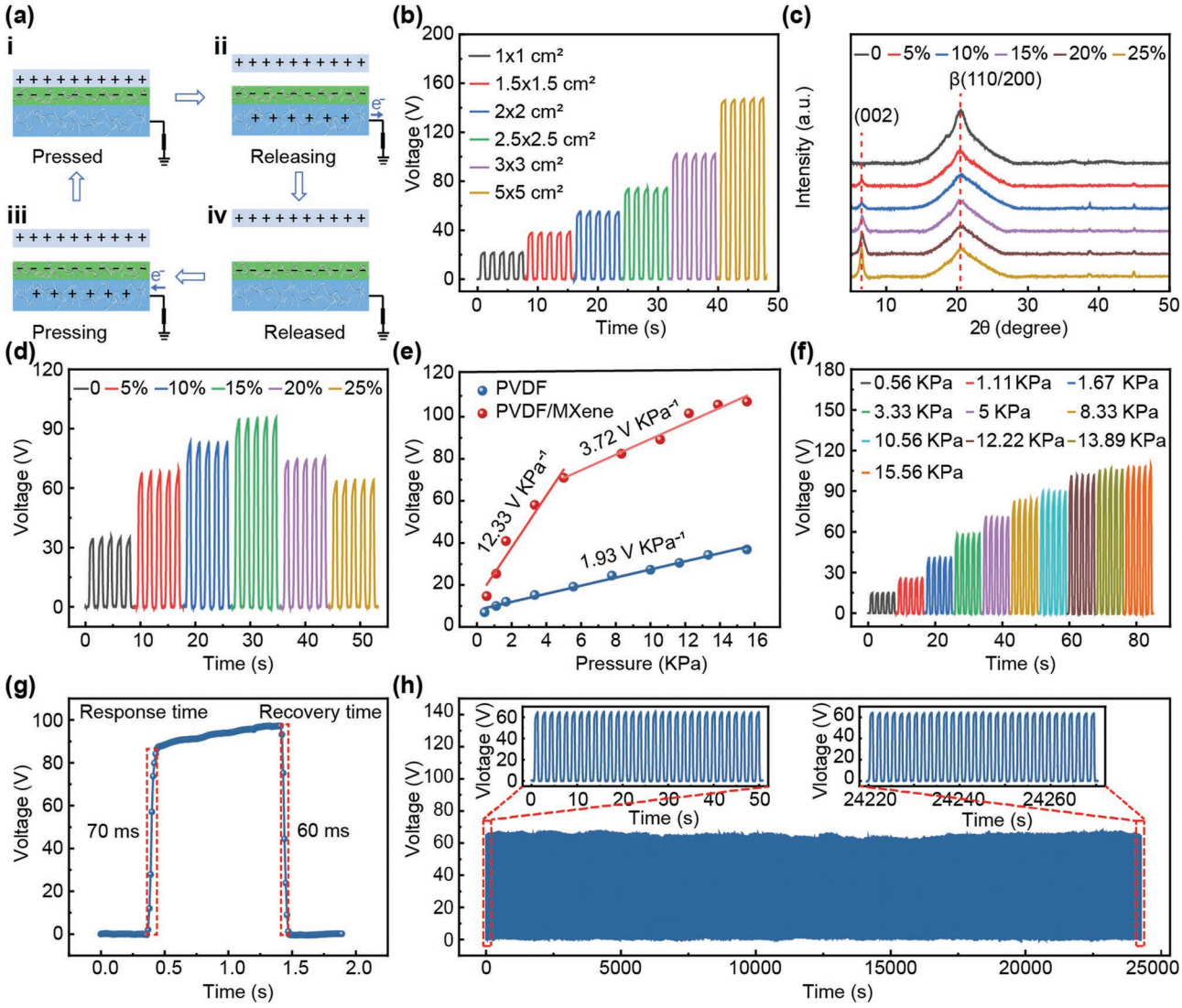

Figure 3. The electrical performance of the LT-TENG. a) Working mechanism of the LT-TENG. b) Open-circuit voltage of the LT-TENG with different sizes. c) The XRD patterns of MXene/PVDF NFs with MXene content from 0% to 25%. d) Open-circuit voltage of the LT-TENG with the MXene content from 0% to 25%. e) Open-circuit voltage of LT-TENG as a function of pressure when the triboelectric layer is PVDF NFs and PVDF/MXene NFs, respectively. f) Dependence of the MXene/PVDF NFs-based LT-TENG output open-circuit voltage on the applied force. g) The response time and recovery time of LT-TENG are 70 and 60 ms, respectively. h) Long-term stability of the fabricated LT-TENG based on MXene/PVDF NFs during 16 000 working cycles.

be spun onto the surface of various textiles with different warp and weft densities, yielding fibrous LT-TENGs with different substrates. Those TENGs can also generate a considerable output of open-circuit voltage (Figure 2e), short-circuit current (Figure S6a, Supporting Information), and short-circuit transfer charge (Figure S6b, Supporting Information). In addition, a large-area TENG with 50 × 20 cm^2 is easily fabricated, with the optical photograph shown in Figure 2fi. Herein, the area is restricted to the roller receiver and can be scale-up if the receiving device is improved by installing a movable pulley to transport blank substrate. At the same time, just because of the large area of the NFs , the LT-TENG can also be directly cut and sewn into various wearable clothing, such as gloves, with corresponding steps shown in Figure 2fii–v. The complete procedure is shown in Movie S1, Supporting Information.

Figure 3a illustrates the working principle of LT-TENG, which operates in a single-electrode mode. When in a close contact state, the PVDF/MXene NFs film gains negative triboelectric charges because of its more robust ability to capture negative charges, whereas the nylon film will be positively charged (Figure 3ai). Once the nylon is moving away, the potential difference will induce instantaneous electron flow from the conductive fabric electrode to the ground (Figure 3aii). The electron flowing continues until the nylon film, and PVDF/MXene film is fully separated (Figure 3aiv). When the nylon film approaches the MXene/PVDF NFs film again, electrons flow from the ground to the conductive fabric, generating a reverse current (Figure 3aiii). Consequently, the continuous contact and separation motion of the LT-TENG will produce an alternating current.[19]

The basic output performance of the LT-TENG can be evaluated by using a linear motor to provide cyclic contact-separation motion. Here, nylon film with strong electro-positivity ability is used as another active friction material for the sensitivity test. As illustrated in Figure 3b, under the maximum contact, the voltage is gradually enhanced (21 to 146 V) as the area increases (1×1 cm^2 to 5×5 cm^2). As shown in Figure S7, Supporting Information, when the size increases, the short-circuit current and short-circuit transfer charge also increase simultaneously. Compared with the size of 1×1 cm^2, the short-circuit current and transferred charge quantity have been boosted by 6 and 7 times, respectively, when the size is 5×5 cm^2. The main reason is that a larger area of TENG leads to a higher transferred charge, generating stronger output performance. Furthermore, considering the size of the device, an appropriate size of LT-TENG with 3×3 cm^2 is adopted to investigate the basic electrical output performance. Subsequently, different mixed mass ratio of $W_{(MXene)}/W_{(PVDF)}$ including 0, 5%, 10%, 15%, 20%, and 25%, has been discussed. XRD analysis of nanofibers with different MXene doping content is performed. As shown in Figure 3c, the strong peak (002) at 6.90° for all samples is from MXene nanosheets. It has been observed that the diffraction peak at (002) is enhanced with the growth of MXene content. On the contrary, the diffraction peak at (110/200) with β-phase is significantly weakened and becomes wider with the increase of content. The XRD result indicates that a higher content of the MXene will result in a lower β-crystallinity of PVDF/MXene NFs. Similarly, the same trend can also be reflected in the Fourier transform infrared (FTIR) spectra (Figure S8, Supporting Information). The PVDF/MXene composite nanofibers and PVDF NFs-all have identical peaks at 840 and 1170 cm^{-1}, which are the characteristic peaks of the β-phase of PVDF. However, with the increase of MXene content, the strength of the absorption band at the β-crystal plane decreases with a mild redshift. In summary, this may be credited to the formation of hydrogen bonds, which happens between PVDF chains with the surface group of MXene, disturbing the balance of the β-phase of PVDF and reducing the crystallinity of nanofibers. In addition, the electroactive β-fraction has been calculated for different MXene contents (Figure S8, Supporting Information).[42] All the above characterization results indicate that MXene is successfully inserted into PVDF chains. According to Figure 3d, the voltage of LT-TENG boosts with the addition of MXene doping content, reaching a maximum at 15%, while with the gradual increase of MXene, the performance is going to decline. The short-circuit current (Figure S9a, Supporting Information), and the transferred charge (Figure S9b, Supporting Information) also have a similar variation tendency. Thus, the optimal mixed ratio of MXene content is 15%, and the output voltage, current, and transferred charge are enhanced by 2.7, 2.5, and 2.4 times compared with TENG based on pristine PVDF, respectively. The decent addition of MXene into PVDF can dramatically improve the performance, which should be ascribed to the high electronegativity of MXene under the existence of F-groups and oxygen-containing functional groups, as well as the enhanced dielectric constant caused by the good electrical conductivity of MXene flakes (Figure S10, Supporting Information). However, redundant MXene in the PVDF/MXene NFs will form a conductive network, expediting leakage transmission and high dielectric loss. Therefore, when the MXene content exceeds the critical value, the output performance of LT-TENG will be degraded. Thus, the LT-TENG is based on PVDF/MXene NFs at the optimal ratio of $W_{(MXene)}/W_{(PVDF)} \approx 15\%$.

To evaluate the sensing performance of LT-TENG, the sensitivity, detecting range, response time, and durability have been investigated. As illustrated in Figure 3e, the relationship between the open-circuit voltage and the externally applied pressure is plotted, and the slop of the curve represents the sensitivity. For the tactile sensor based on PVDF NFs, there is one linear region with a sensitivity of 1.93 V KPa^{-1} over the detecting range of 0–16 KPa. For the LT-TENG fabricated by PVDF/MXene NFs, there exist two linear regions (region I and region II). Under low pressure, a tiny change in external pressure will cause a large contact area variation due to the fibrous structure of PVDF/MXene NFs, resulting in a large change in the output. Thus, in linear region I, the sensitivity is relatively as high as 12.33 V KPa^{-1} below 5 kPa, which is 6.4 times as high as pure PVDF. In linear region II, under high pressure, the variation in the fibrous structure becomes slow, generating a lower sensitivity of 3.72 V KPa^{-1} over 5–16 kPa, which is still 1.9 times as high as pure PVDF. According to the results, the sensitivity of the device is optimal at pressures between 0 and 16 kPa. This shows that the addition of MXene improves the sensitivity of the LT-TENG in general, especially in the lower pressure range. Furthermore, the voltage (Figure 3f), current (Figure S11a, Supporting Information), and charge (Figure S11b, Supporting Information) of the LT-TENG at different pressures from 0.56 to 15.56 KPa are displayed. Obviously, when the applied pressure increases, the voltage, current, and charge gradually increase from 15 to 108 V, 0.05 to 0.38 μA, and 5.2 to 35 nC, respectively. Those output signals all increase more rapidly in the lower pressure range and slowly in the larger pressure range. As for the reaction time of the LT-TENG, it can be observed that the response time is 70 ms and the recovery time is 60 ms under the stress of 15 KPa, as shown in Figure 3g. In order to achieve wearability, durability is also an important indicator in practical applications. The LT-TENG has excellent durability, which is not only convenient but also can reduce the cost of use. Figure 3h shows 16 000 cycles of TENG under a continuous press at a 4 kPa, the output voltage is almost constant according to the result in the first 50 s and the last 50 s (inset in Figure 3h), demonstrating superior durability of the LT-TENG.

Except for a self-powered sensor, the LT-TENG is capable of collecting mechanical energy and converting it into electricity. Different resistors (10^3–10^{11} Ω) can be served as external loads to evaluate the output power density of the LT-TENG. According to Ohm's law, it can be seen that as the increase of load resistance, the voltage rises while the current gradually decreases (**Figure 4**a). The instantaneous power density is calculated by Equation (1).

$$W = V^2 RS \tag{1}$$

where V is the corresponding voltage, R is the external load resistance, and S is the size of the LT-TENG (3×3 cm^2). The LT-TENG can achieve a maximum instantaneous power density value of 12.6 mW m^{-2} when the load resistance is 500 MΩ, with results displayed in Figure 4b. In addition, a self-powered

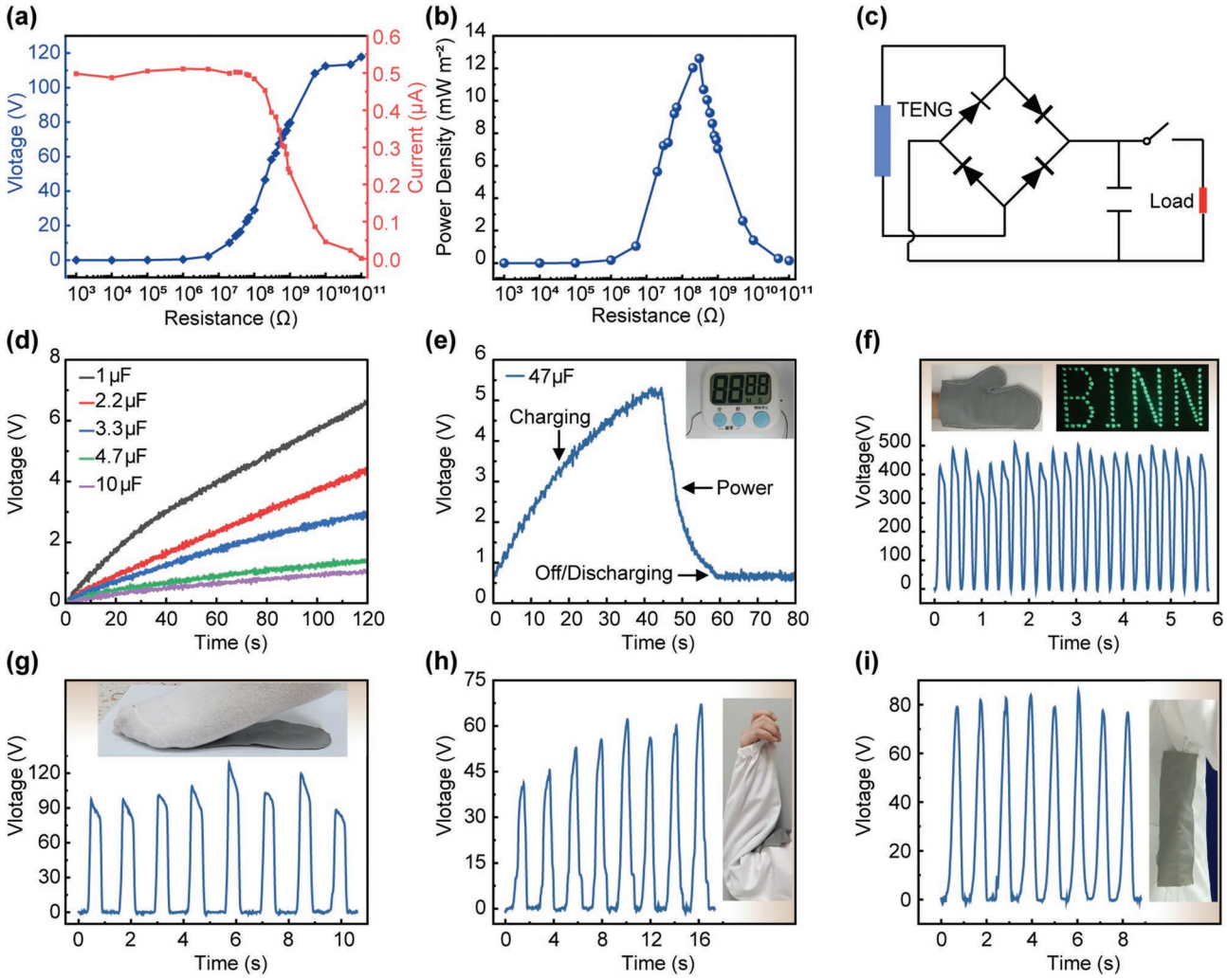

Figure 4. It demonstrates that the LT-TENG can be used for bio-energy harvesting. a) Voltage and current of LT-TENG under different external load resistance. b) Power density of the LT-TENG with load resistance. c) The equivalent electrical circuit of the self-powered system. d) Charging schematic of the LT-TENG at 1, 2.2, 3.3, 4.7, and 10 μF capacitance capacity. e) The characteristics of charging and discharging curves of the capacitors for operating a commercial timer (inset displays the turn ON condition timer). f) Output voltage signal when tapped when the LT-TENG is cut to a glove (inset shows an optical photograph of the glove and the lit LED). Images and output voltage of the LT-TENG are fixed in different locations on the human body: g) under the foot, h) inset the elbow joint, and i) under the arm.

power supply system is constructed to investigate the potential of self-powered applications of the LT-TENG. According to Figure 4c, the equivalent circuit contains a load resistor, a commercial capacitor, a rectifier bridge, and an LT-TENG. The generated AC power from the LT-TENG will be stored in the commercial capacitor through the rectifier bridge. As seen in Figure 4d, it's the charging capability of the LT-TENG with sizes of 3×3 cm^2 for different capacitors (1, 2.2, 3.3, 4.7, and 10 μF). It can be observed that the charging rate will slow down with the increase of capacitance. The electric power stored in the capacitor can be utilized to drive some small electronic devices. As shown in Figure 4e, the stored electricity from a 47 μF capacitor, which is charged by the LT-TENG (with a size of 10×10 cm^2) over 43 s, can light up a timer for more than 10 s. Furthermore, tapping the table with gloves made of LT-TENG can generate an output voltage of ≈500 V (Figure 4f), which can light up the 113 LEDs placed into the letters "BINN" (Movie S2, Supporting Information). Those results demonstrate the LT-TENG can be a reliable power source to support and drive different electronics. Alternatively, the LT-TENG can harvest the unordered biomechanical energy from our daily life when combined with the human body. For example, the LT-TENG can be tailored into a shoe insole, generating principle ≈120 V electricity when walking (Figure 4g). The LT-TENG can produce about 90 and 80 V, respectively, by the up-down movement of the arm and the elbow. This sustainable LT-TENG can be an energy harvester by collecting daily biomechanical energy and generating effective electrical output to support various electronics, demonstrating great potential in self-powered systems and wearable electronics.

The LT-TENG can not only be used for large-area power harvesters but also can be integrated for self-powered tactile sensing. When used as sliding perceiving, the performance of the LT-TENG with the size of 1×1 cm^2 is investigated at a

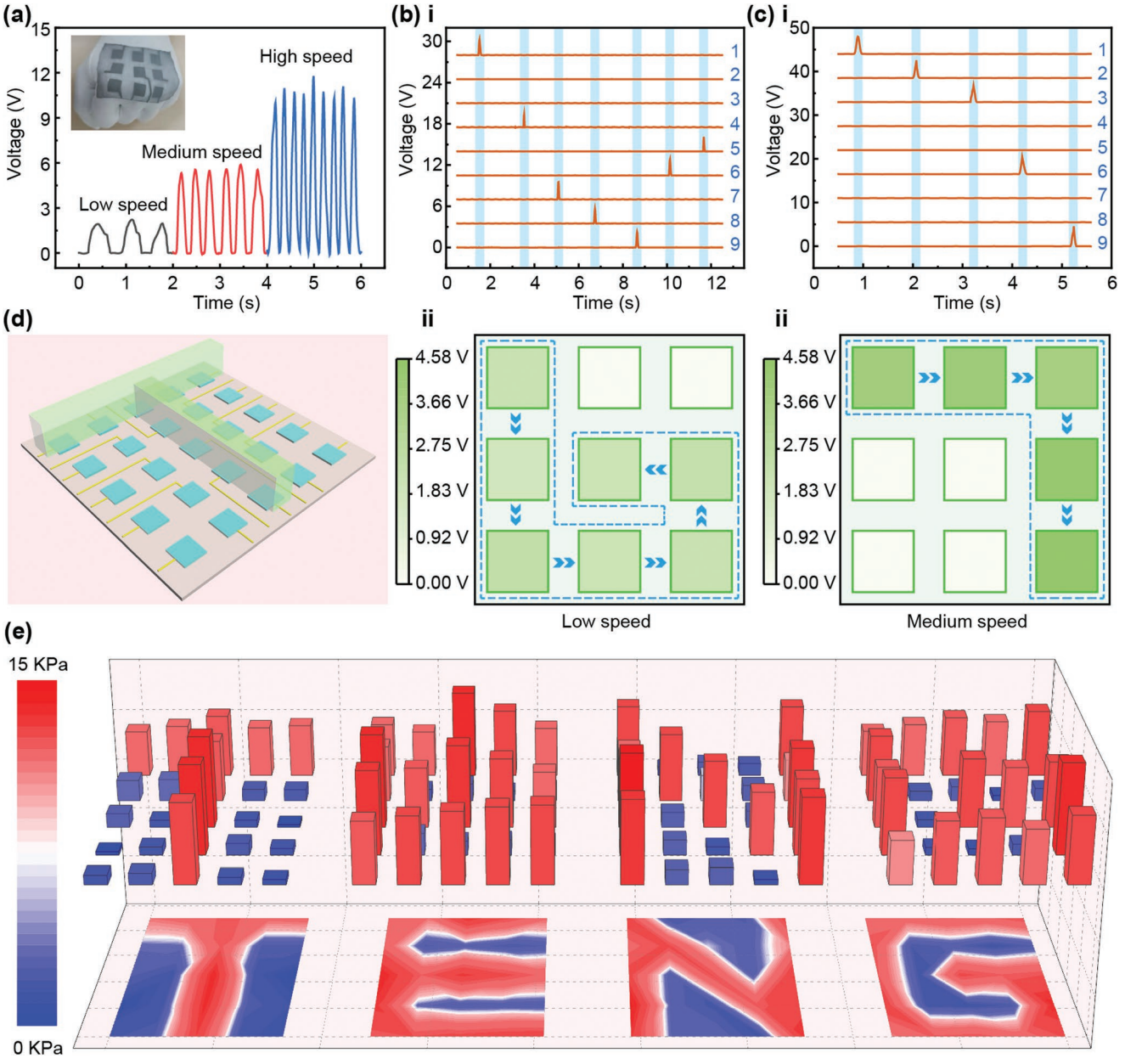

Figure 5. Pressure mapping of sliding and stress sensing arrays based on LT-TENG. a) Output voltage signal when sliding a single LT-TENG-based sensor using the finger at low, medium, and fast speeds (inset is a photo of the 3 × 3 pixels sensing array integrated into the glove). The voltage signals of the 3 × 3 pixels sensing array (collected using a synchronous data acquisition card) and the slide traces bii) "6" and cii) "7" are slid using the finger at bi) low and ci) medium speeds. d) Schematic diagram of applying stress to a flexible tactile sensor array with 5 × 5 pixels using the letter "T." e) Output voltage and voltage mapping of the 5 × 5 arrays using the letters "T," "E," "N," and "G."

slow, medium, and fast speed by the human finger, respectively (**Figure 5**a). As the sliding speed increases, the output voltage of the sensor is also enhanced. In order to address the detection limitations of a single sensing unit and provide more comprehensive information, multiple sensing units are concentrated on clothing to form an array, which can achieve haptic mapping of 2D regions. A 3 × 3 pixels sensing array is integrated into a glove, as shown in the inset of Figure 5a. When wearing the packaged glove, a number "6" and "7" is drawn by a finger at a slow and medium speed, with corresponding results illustrated in Figure 5b,c. It can be observed that a higher speed leads to a higher multi-channel output signal (Figure 5bi,ci), which is consistent with the above results. At the same time, the trajectory mapping (Figure 5bii,cii) of different sliding paths of the finger can be obtained. In addition to sliding sensing, the self-powered sensor array also responds to external pressure stimulation. Figure 5d illustrates the use of the letter "T" to apply stress to a flexible tactile sensor array with 5 × 5 pixels. A real picture of a 5 × 5 array is shown in Figure S12, Supporting Information. Movie S3, Supporting Information, is a demonstration

of 5 × 5 array pressure sensing. Different letters ("T," "E," "N," and "G") are used to apply external pressure stimulus, with a pressure mapping diagram illustrated in Figure 5e. The specific pressure analysis is shown in Figure S13, Supporting Information. It can be seen that the array sensor can accurately detect the contact position between the object and its surface. These results show that the LT-TENG is capable of mapping external stimuli and acquiring electrical energy by sensing the outside world through the skin, enabling potential applications of human–computer interaction.

3. Conclusions

In summary, we designed an all-fibrous, washable, superhydrophobic, and self-powered LT-TENG by integrating MXene nanosheets into PVDF nanofibers based on a new SBS technology, which enables the LT-TENG with the considerable area and potential tailorability. This SBS approach owns the merits of easy operation, high security, and good universality when used to fabricate devices with nanofibers. Furthermore, MXene nanosheets mixed into PVDF are utilized to enhance the capability of LT-TENG. When compared with the TENG based on pristine PVDF NFs, TENG composed of PVDF/MXene NFs with the optimal mixed concentrate of 15% can generate a higher output voltage, current, and transferred charge by 2.7, 2.5, and 2.4 times, respectively. As a self-powered sensor, it can detect external pressure over 16 KPa with a relatively high sensitivity of 12.33 V KPa^{-1} and provide a power density of 12.6 mW m^{-2} with optimal matching resistance of 500 MΩ. Simultaneously, this LT-TENG not only can be used as a biomechanical energy harvester and a sustainable power source for driving some electronic devices but also serve as a tactile sensor array for pressure mapping and sliding perceiving, providing significant potential applications in wearable devices, soft robotics, and human–computer interaction.

4. Experimental Section

Materials: Ti_3AlC_2 MAX (200 mesh, 98%) phase precursor was purchased from Forsman. Hydrochloric acid (HCl, 36–38%) was purchased from Modern Oriental (Beijing) Technology Development Co., Ltd. Lithium fluoride (LiF, 99%), PVDF (Mw ≈400 000), and *N*, *N*-dimethylformamide (DMF, 99.9%, GC) used in this work were purchased from Aladdin. Acetone (CH_3COCH_3, 99.5%, AR) was purchased from Xilong Scientific Co., Ltd. All materials were used directly, without further purification. Nylon films were purchased from Beijing Tianhong Shengshi Trade Co., Ltd. Fabrics of different warp and weft densities were purchased from local wholesale fabric markets.

Synthesis of $Ti_3C_2T_x$ MXene Nanosheets: Ti_3AlC_2 MAX phase precursor. At first, LiF (1.65 g) was added to HCl (25 mL, 6 M) and stirred for 10 min, and then Ti_3AlC_2 (1.25 g) was slowly added while stirring. Subsequently, it was stirred at 35 °C for 48 h with a magnetic stirrer at 250 rpm min^{-1}. The resulting mixture was washed with deionized water (DI), centrifuged at 8000 rpm for 8 min, repeated washing, and centrifuged until the pH approached 6. Finally, the resulting suspension was vacuum filtered, and the MXene film was obtained. It was dried at 60 °C for 12 h and grounded into a powder for backup.

Preparation of the PVDF/MXene Mixed Solution: First, PVDF particles were dissolved in acetone and DMF at a mass ratio of 0.75:1:4 and stirred magnetically at 70 °C and 1000 rpm for 3 h until they completely dissolved. Then, MXene powder was mixed with PVDF solution, stirred at 25 °C for 22 h, and sonicated for 2 h to obtain the PVDF/MXene mixed solution. The mass percentages of MXene powder were 5%, 10%, 15%, 20%, and 25%, respectively.

Fabrication of the Large-Area Tailorable TENG: LT-TENG was prepared in one step by the SBS method, as shown in Figure 1a. First, the PVDF/MXene mixture was loaded into a 5 mL spiral syringe for air spinning to obtain PVDF/MXene NFs. The spinning rate was controlled at 1.5 mL h^{-1}, the airflow rate was 40 L min^{-1}, and the solution and airflow temperature were 36 and 45 °C, respectively. Second, conductive fabrics were breathable and had high electrical conductivity, which could be used as electrodes for wearable devices. The conductive fabric was cut to 20 × 50 cm and wrapped around the drum as a collector for the NFs. Finally, the baking lamp was turned on and after drying for 2 h, the LT-TENG was directly obtained and the LT-TENG could be cut into different shapes.

Measurements and Characterizations: The structure and morphology of MXene flakes and PVDF/MXene NFs were characterized by scanning electron microscopy (FEI Nova, NanoSEM 450), and the NFs were analyzed by elemental dispersion using EDS (FEI Quanta 450). The crystal structures of pure MXene and NFs were determined by an XRD (Xpert3 Powder). The FTIR spectroscopy (Bruker VERTEX80v) served as a study of the composition of NFs using a linear motor (LinMot) to provide the periodic reciprocating motion of the LT-TENG. The force signal was detected by a hexagonal force and torque sensor (FT28194). The voltage, current, and transferred charge signals were recorded by an electrometer (Keithley 6514).

Supporting Information

Supporting Information is available from the Wiley Online Library or from the author.

Acknowledgements

H.Y.X. and J.T. contributed equally to this work. The authors thank the support of the National Natural Science Foundation of China (Nos. U20A20166, 52125205, and 52192614), the National Key R&D Program of China (2021YFB3200302 and 2021YFB3200304), the Natural Science Foundation of Beijing Municipality (Z180011 and 2222088), the Shenzhen Science and Technology Program (Grant No. KQTD20170810105439418), the China Postdoctoral Science Foundation (2021M690108), and the Fundamental Research Funds for the Central Universities.

Conflict of Interest

The authors declare no conflict of interest.

Data Availability Statement

The data that support the findings of this study are available from the corresponding author upon reasonable request.

Keywords

large area, polyvinylidene fluoride/MXene nanofibers, solution blow spinning, triboelectric nanogenerators

Received: April 21, 2022
Revised: June 15, 2022
Published online:

[1] Y. Liu, R. Bao, J. Tao, J. Li, M. Dong, C. Pan, *Sci. Bull.* **2020**, *65*, 70.
[2] C. Wang, C. Pan, Z. Wang, *ACS Nano* **2019**, *13*, 12287.
[3] Y. Ling, T. An, L. Yap, B. Zhu, S. Gong, W. Cheng, *Adv. Mater.* **2020**, *32*, 1904664.
[4] R. Zhu, Z. Li, G. Deng, Y. Yu, J. Shui, R. Yu, C. Pan, X. Liu, *Nano Energy* **2022**, *92*, 106700.
[5] H. Liu, Q. Li, Y. Bu, N. Zhang, C. Wang, C. Pan, L. Mi, Z. Guo, C. Liu, C. Shen, *Nano Energy* **2019**, *66*, 104143.
[6] S. Wan, N. Wu, Y. Ye, S. Li, H. Huang, L. Chen, H. Bi, L. Sun, *Small Struct.* **2021**, *2*, 2100105.
[7] J. Ren, W. Zhang, Y. Wang, Y. Wang, J. Zhou, L. Dai, M. Xu, *InfoMat* **2019**, *1*, 396.
[8] G. Ge, Y. Lu, X. Qu, W. Zhao, Y. Ren, W. Wang, Q. Wang, W. Huang, X. Dong, *ACS Nano* **2020**, *14*, 218.
[9] G. Ge, W. Yuan, W. Zhao, Y. Lu, Y. Zhang, W. Wang, P. Chen, W. Huang, W. Si, X. Dong, *J. Mater. Chem. A* **2019**, *7*, 5949.
[10] K. Zhou, Y. Zhao, X. Sun, Z. Yuan, G. Zheng, K. Dai, L. Mi, C. Pan, C. Liu, C. Shen, *Nano Energy* **2020**, *70*, 104546.
[11] J. Sun, Y. Chang, L. Dong, K. Zhang, Q. Hua, J. Zang, Q. Chen, Y. Shang, C. Pan, C. Shan, *Nano Energy* **2021**, *86*, 106077.
[12] Q. Hua, J. Sun, H. Liu, R. Bao, R. Yu, J. Zhai, C. Pan, Z. L. Wang, *Nat. Commun.* **2018**, *9*, 244.
[13] J. Li, Z. Yuan, X. Han, C. Wang, Z. Huo, Q. Lu, M. Xiong, X. Ma, W. Gao, C. Pan, *Small Sci.* **2022**, *2*, 2100083.
[14] Y. Zhao, W. Gao, K. Dai, S. Wang, Z. Yuan, J. Li, W. Zhai, G. Zheng, C. Pan, C. Liu, C. Shen, *Adv. Mater.* **2021**, *33*, 2102332.
[15] F. Fan, Z. Tian, Z. Wang, *Nano Energy* **2012**, *1*, 328.
[16] K. Dong, Z. Wu, J. Deng, A. C. Wang, H. Zou, C. Chen, D. Hu, B. Gu, B. Sun, Z. L. Wang, *Adv. Mater.* **2018**, *30*, 1804944.
[17] X. Li, Y. Wang, Y. Zhao, J. Zhang, L. Qu, *Small Struct.* **2021**, *3*, 2100124.
[18] W. Guo, X. Li, M. Chen, L. Xu, L. Dong, X. Cao, W. Tang, J. Zhu, C. Lin, C. Pan, Z. L. Wang, *Adv. Funct. Mater.* **2014**, *24*, 6691.
[19] X. Lu, L. Zheng, H. Zhang, W. Wang, Z. L. Wang, C. Sun, *Nano Energy* **2020**, *78*, 105359.
[20] M. Shi, H. Wu, J. Zhang, M. Han, B. Meng, H. Zhang, *Nano Energy* **2017**, *32*, 479.
[21] P. Tan, X. Han, X. Qu, J. Xue, T. Li, Y. Wang, R. Luo, X. Cui, Y. Xi, L. Wu, B. Xue, D. Luo, Y. Fan, X. Chen, Z. Li, Z. Wang, *Adv. Mater.* **2022**, *34*, 2200793.
[22] X. Qu, J. Xue, Y. Liu, W. Rao, Z. Liu, Z. Li, *Nano Energy* **2022**, *98*, 107324.
[23] Y. Cao, Y. Yang, X. Qu, B. Shi, L. Xu, J. Xue, C. Wang, Y. Bai, Y. Gai, D. Luo, Z. Li, *Small Methods* **2022**, *6*, 2101529.
[24] Z.-L. Tan, J.-X. Wei, Y. Liu, F. u. Zaman, W. Rehman, L.-R. Hou, C.-Z. Yuan, *Rare Met.* **2021**, *41*, 775.
[25] Q. Zhao, Y. Zhang, Z. Duan, S. Wang, C. Liu, Y. Jiang, H. Tai, *Rare Met.* **2020**, *40*, 1459.
[26] Z. Qiu, Y. Bai, Y. Gao, C. Liu, Y. Ru, Y. Pi, Y. Zhang, Y. Luo, H. Pang, *Rare Met.* **2021**, *41*, 1101.
[27] A. Ahmed, S. Sharma, B. Adak, M. M. Hossain, A. M. LaChance, S. Mukhopadhyay, L. Sun, *InfoMat* **2022**, *4*, e12295.
[28] H. Liu, X. Chen, Y. Zheng, D. Zhang, Y. Zhao, C. Wang, C. Pan, C. Liu, C. Shen, *Adv. Funct. Mater.* **2021**, *31*, 2008006.
[29] Y. Lu, X. Qu, W. Zhao, Y. Ren, W. Si, W. Wang, Q. Wang, W. Huang, X. Dong, *Research* **2020**, *2020*, 2038560.
[30] Y. Jiang, K. Dong, X. Li, J. An, D. Wu, X. Peng, J. Yi, C. Ning, R. Cheng, P. Yu, Z. L. Wang, *Adv. Funct. Mater.* **2020**, *31*, 2005584.
[31] P. Bai, G. Zhu, Q. Jing, J. Yang, J. Chen, Y. Su, J. Ma, G. Zhang, Z. L. Wang, *Adv. Funct. Mater.* **2014**, *24*, 5807.
[32] M. He, W. Du, Y. Feng, S. Li, W. Wang, X. Zhang, A. Yu, L. Wan, J. Zhai, *Nano Energy* **2021**, *86*, 106058.
[33] K. Dong, J. Deng, Y. Zi, Y. C. Wang, C. Xu, H. Zou, W. Ding, Y. Dai, B. Gu, B. Sun, Z. L. Wang, *Adv. Mater.* **2017**, *29*, 1702648.
[34] S. Zhao, J. Wang, X. Du, J. Wang, R. Cao, Y. Yin, X. Zhang, Z. Yuan, Y. Xing, D. Y. H. Pui, C. Li, *ACS Appl. Energy Mater* **2018**, *1*, 2326.
[35] J. Huang, Y. Hao, M. Zhao, W. Li, F. Huang, Q . Wei, *ACS Appl. Mater. Interfaces* **2021**, *13*, 24774.
[36] B. Ye, C. Jia, Z. Li, L. Li, Q. Zhao, J. Wang, H. Wu, *J. Appl. Polym. Sci.* **2020**, *137*, 49103.
[37] Y. Gao, J. Zhang, Y. Su, H. Wang, X. X. Wang, L. P. Huang, M. Yu, S. Ramakrishna, Y. Z. Long, *Mater. Horiz.* **2021**, *8*, 426.
[38] H. Zhang, R. Wang, P. Li, L. Jia, F. Wang, Y. Liu, H. Wang, L. Yu, B. Li, *ACS Appl. Mater. Interfaces* **2021**, *13*, 6631.
[39] Z. Li, J. Song, Y. Long, C. Jia, Z. Liu, L. Li, C. Yang, J. Liu, S. Lin, H. Wang, Y. Liu, M. Fang, H. Wu, *Nano Res.* **2020**, *13*, 861.
[40] R. Q. Liu, X. X. Wang, J. Fu, Q. Q. Zhang, W. Z. Song, Y. Xu, Y. Q. Chen, S. Ramakrishna, Y. Z. Long, *Nanomaterials* **2019**, *9*, 1090.
[41] B. Tandon, P. Kamble, R. T. Olsson, J. J. Blaker, S. H. Cartmell, *Molecules* **2019**, *24*, 1903.
[42] M. Tayyab, J. Wang, J. Wang, M. Maksutoglu, H. Yu, G. Sun, F. Yildiz, M. Eginligil, W. Huang, *Nano Energy* **2020**, *77*, 105178.